



## Adding Fe/dicyandiamide to Co-MOF to greatly improve its ORR/OER bifunctional electrocatalytic activity

Can Fang <sup>a</sup>, Xiangmei Tang <sup>a</sup>, Qingfeng Yi <sup>a,b,\*</sup>

<sup>a</sup> School of Chemistry and Chemical Engineering, Hunan University of Science and Technology, Xiangtan, Hunan 411201, PR China

<sup>b</sup> Hunan Provincial Key Lab of Advanced Materials for New Energy Storage and Conversion, Xiangtan 411201, PR China



### ARTICLE INFO

#### Keywords:

Metal organic framework  
Oxygen reduce reaction  
Oxygen evolution reaction  
Carbon nanotubes  
New (n)-diamond

### ABSTRACT

Exploring efficient non-precious metal oxygen electrocatalysts for oxygen reduction/evolution reactions (ORR/OER) is of great importance in electrochemical energy conversion devices like metal-air battery. Among them, carbon-based composites derived from metal-organic framework (MOF) exhibit excellent catalytic performance in ORR/OER. In this paper, Co-MOF-67 was firstly prepared, and then mixed with  $\text{FeCl}_3 \cdot 6 \text{ H}_2\text{O}$  and dicyandiamide, followed by a one-step pyrolysis to obtain bamboo-like nitrogen-doped carbon nanotubes. For the samples, Fe and Co nanoparticles were encapsulated in the front end of the carbon nanotubes and the presence of new (n)-diamond carbon was unexpectedly found. The obtained catalyst (FeCo@CNTs-60) has an onset potential of 1.04 V for ORR in alkaline solution, which is close to the commercial Pt/C (40 wt% Pt) of 1.05 V. The onset potential of 1.02 V in quasi-neutral solution exceeds that of Pt/C of 0.99 V. In addition, FeCo@CNTs-60 exhibited a low potential difference of 0.81 V between OER and ORR potentials. The alkaline zinc-air batteries, fabricated with the sample as the electrocatalyst of air electrode, exhibit higher peak power density and stability than Pt/C, while the rechargeable batteries present superior cycling discharge/charge stability at  $5 \text{ mA} \cdot \text{cm}^{-2}$  and  $10 \text{ mA} \cdot \text{cm}^{-2}$ . In particular, the battery with FeCo@CNTs-60 was conducted for continuous over 1300 h of ultra long-term cycle charging / discharging test at a current density of  $5 \text{ mA} \cdot \text{cm}^{-2}$ , and it reveals excellent stability with high voltage efficiency and also presents superior cycle charging / discharging stability after replacing the Zn plates and electrolyte.

### 1. Introduction

Traditional fossil energy has made an indelible contribution to the development of human society; however, fossil energy resources are limited and their excessive use has brought about increasingly serious environmental pollution problems [1,2]. The development of new, efficient and environmentally friendly renewable energy sources is an important solution to achieve sustainable development and solve environmental pollution. Zinc-air batteries (ZABs) have received much attention due to their environmental friendliness, high theoretical specific energy density, low preparation cost and safety in use [3,4]. The slow kinetics of oxygen reduction reaction (ORR) and oxygen evolution reaction (OER) on the cathode of rechargeable ZABs is however, a crucial factor limiting the efficiency of batteries [5–7]. Although conventional noble metal catalysts such as Pt-based and Ir-based catalysts are excellent ORR/OER catalysts respectively, the low storage capacity of Pt and Ir on earth, the high preparation cost of noble metal catalysts

and the poor durability in use limit their large-scale commercial application [8,9]. Therefore, the development of low-cost, high catalytic activity and high durability bifunctional ORR/OER catalysts is essential for rechargeable ZABs.

Until now, non-precious metal (such as Mn, Fe, Co and Ni) loaded carbon-based materials have received much attention due to their low cost, high catalytic activity and good stability. Non-precious metal catalysts based on N-doped carbon materials combined with Fe or Co exhibit high ORR activity, which is attributed to the structural advantages and the increase of active sites due to doping [10,11]. However, few bifunctional catalysts with ORR and OER are available, as a single active site usually serves only one side (ORR or OER) of the catalytic process. According to the calculations based on density functional theory (DFT) reported by Calle-Vallejo et al., the Fe and Mn active sites have high catalysis for ORR, while the Co active site is biased toward OER catalysis [12]. Bifunctional catalysts require the synergy and complementarity of multiple sites, and it is crucial to design a rational

\* Corresponding author at: School of Chemistry and Chemical Engineering, Hunan University of Science and Technology, Xiangtan, Hunan 411201, PR China.  
E-mail address: [yqfyy2001@hnust.edu.cn](mailto:yqfyy2001@hnust.edu.cn) (Q. Yi).

doping scheme to integrate multiple active sites [13]. Generally, bimetallic catalysts can produce a synergistic effect and thus bring more active sites, enhancing their ORR electroactivity and also strengthening their OER performance. This results in the possibility for the synthesis of the bifunctional catalysts with both highly efficient ORR and OER electroactivity. For example, Duan et al. obtained  $\text{Fe}^{3+}$  encapsulated zeolitic imidazolate framework-8/67 by introducing  $\text{Co}^{2+}$  and  $\text{Fe}^{3+}$  with  $\text{SiO}_2$  as a template to obtain FeCo co-doped bifunctional catalysts with a graded spherical structure, and Shen et al. synthesized carbon hollow spheres and carbon nanotubes (CNTs) coexisting bifunctional catalysts by introducing  $\text{Co}^{2+}$  and  $\text{Ni}^{+}$  using  $\text{SiO}_2$  as a template [14,15]. On the other hand, a reasonable carbon structure can not only bring high specific surface area and increase the active sites, but also protect the doped atoms and bring good stability [16]. The common carbon structures include graphene, CNTs, carbon nanosheets and carbon hollow spheres, among which the hollow tubular structure of CNTs can shorten the mass transfer distance and achieve fast electron transport [17]. Notably, N-doped CNTs have more excellent electrocatalytic performance, which is attributed to that N doping alters the structural properties of CNTs and improves the ORR/OER activity [18,19].

Metal organic frameworks (MOFs) are 3D porous materials formed by self-assembly of organic ligands and metal ions or clusters through coordination bonding, with high specific surface area and homogeneous dispersion of metal ions [20,21]. MOF-derived carbon materials can possess the advantages of MOFs themselves [22]. MOF materials can be pyrolyzed to form porous materials bringing large specific surface area and abundant pore channels, which are conducive to the exchange and transfer of reaction substances. Also, the active sites after pyrolysis are uniformly distributed among the N-doped skeleton [23]. In particular, the preparation of N-doped carbon nanomaterials using zeolite imidazolium ester backbone (ZIF) among MOF structures as precursors is more effective [24]. For example, the pyrolysis of ZIF-67 in a nitrogen atmosphere can produce Co nanoparticles and N-doped carbon substrates, bringing about Co active sites and N-coordinated Co active sites, etc. However, catalysts prepared by single ZIF-67 pyrolysis will suffer from dissociation and aggregation of Co nanoparticles, resulting in the reduced catalytic activity and stability. So, it is a feasible solution to fix and protect the metal active sites by rational design of carbon-based materials [25,26]. In the recent study, Ma et al. prepared nitrogen-doped bamboo-like CNTs with an excellent ORR activity and methanol resistance using single-source dicyandiamide-based Co-MOF as a template [27]. The Co active site was wrapped around the front end of the CNTs, which acted as a protective and immobilizing agent.

In this paper, we obtained Fe and Co co-doped CNTs by one-step pyrolysis based on the principle that ZIF-67 was induced to form CNTs by the presence of  $\text{Fe}^{3+}$  and DCD. We explored the effect of adding  $\text{Fe}^{3+}$  before and after the formation of ZIF-67 and found that adding  $\text{Fe}^{3+}$  after the formation of ZIF-67 could be more conducive to inducing the growth of CNTs and effectively improve the ORR performance. Further, a series of catalysts FeCo@CNTs-x were obtained through changing the ratio of Fe and Co, among which FeCo@CNTs-60 showed the best ORR and OER performance. The morphological structure of the FeCo@CNTs-60 is almost entirely bamboo-like carbon nanotubes with Fe and Co wrapped by a multilayer graphite at the front end of the nanotube. FeCo@CNTs-60 exhibits good ORR performance and stability under alkaline and neutral conditions, and the alkaline ZABs assembled by FeCo@CNTs-60 exhibits a higher power density of  $268.3 \text{ mW}\cdot\text{cm}^{-2}$  than Pt/C, while the charge/discharge efficiency and cycling stability are also higher than the battery with Pt/C+IrO<sub>2</sub>. The contributions of Fe and Co to ORR/OER activity were further investigated by density functional theory.

## 2. Experimental section

### 2.1. Materials

$\text{Co}(\text{NO}_3)_2\cdot 6 \text{ H}_2\text{O}$  ( $\geq 99.0\%$ ) was purchased from Guangdong Taishan Chemical Factory (Taishan, China),  $\text{Fe}(\text{NO}_3)_3\cdot 9 \text{ H}_2\text{O}$  ( $\geq 98.5\%$ ) was purchased from Tianjin Daman Chemical Reagent Factory (Tianjin, China), Anhydrous methanol ( $\geq 99.5\%$ ) was purchased from West Long Chemical Plant (Shantou, China), 2-Methylimidazole (98.0 %) and  $\text{IrO}_2$  (99.9 %) were purchased from Shanghai Aladdin Biochemical Technology Co. Ltd. (Shanghai, China), Anhydrous ethanol ( $\geq 99.7\%$ ) was obtained from Guangdong Guanghua Sci-Tech Co. Ltd. (Shantou, China), Dicyandiamide ( $\geq 98.0\%$ ) and Nafion solution (5 %) were obtained from Sinopharm Chemical Reagent Co. Ltd (Shanghai, China),  $\text{FeCl}_3\cdot 6 \text{ H}_2\text{O}$  ( $\geq 99.0\%$ ), Commercial Pt/C (40 %) was obtained from Shanghai Qunyi Energy Equipment Co. Ltd (Shanghai, China), Carbon cloth (thickness=0.35 mm) was obtained from Shanghai Jose Electric Co. Ltd. (Shanghai, China), experimental water is ultrapure water ( $18.2 \text{ M}\Omega\cdot\text{cm}$ ).

### 2.2. Synthesis of ZIF-67 and FeCo-MOF

The synthesis of ZIF-67 was referred to the published literature [28, 29]. 8 mmol of  $\text{Co}(\text{NO}_3)_2\cdot 6 \text{ H}_2\text{O}$  and 32 mmol of 2-Methylimidazole were dissolved in 140 mL and 180 mL of methanol solution, respectively, and then the methanol solution containing 2-Methylimidazole was poured into the methanol solution containing  $\text{Co}(\text{NO}_3)_2\cdot 6 \text{ H}_2\text{O}$ . The resulting mixed solution was stirred for 10 min and then allowed to stand at room temperature for 24 h. The precipitate was collected by centrifugation and washed three times with methanol. Finally, it was dried in an oven at 60 °C. As a comparison, FeCo-MOF was also synthesized by using the same steps as the ZIF-67 except that an additional 8 mmol of  $\text{Fe}(\text{NO}_3)_3\cdot 9 \text{ H}_2\text{O}$  was added to 140 mL of methanol solution containing 8 mmol of  $\text{Co}(\text{NO}_3)_2\cdot 6 \text{ H}_2\text{O}$ .

### 2.3. Synthesis of Co@NTu-CNsh

300 mg of ZIF-67 and 1.5 g of DCD were dissolved in 50 mL of ethanol solution, sonicated for 10 min, and then transferred to an oven at 60 °C for drying. The resulting solid mixture was placed in a tube furnace and pyrolyzed at 800 °C for 2 h in a  $\text{N}_2$  atmosphere. The obtained sample was recorded as Co@NTu-CNsh.

### 2.4. Synthesis of FeCo@CNsh

300 mg of FeCo-MOF and 1.5 g of DCD were dissolved in 50 mL of ethanol solution, sonicated for 10 min, and then transferred to an oven at 60 °C for drying. The obtained solid mixture was placed in a tube furnace and pyrolyzed at 800 °C for 2 h in  $\text{N}_2$  atmosphere. The obtained sample was recorded as FeCo@CNsh.

### 2.5. Synthesis of FeCo@CNTs-x

300 mg of ZIF-67 and 20 mg of  $\text{FeCl}_3\cdot 6 \text{ H}_2\text{O}$  were dissolved in 50 mL of ethanol solution and sonicated for 10 min, followed by adding 1.5 g of DCD to the mixed solution and sonicated for 10 min, and then transferred to an oven at 60 °C for drying. The obtained solid mixture was placed in a tube furnace and pyrolyzed at 800 °C for 2 h in a  $\text{N}_2$  atmosphere. The obtained samples were recorded as FeCo@CNTs-20. In order to explore the effect of Fe content on the performance of the sample, different masses of  $\text{FeCl}_3\cdot 6 \text{ H}_2\text{O}$  (40 mg, 60 mg and 80 mg) were applied to obtain the corresponding samples recorded as FeCo@CNTs-40, FeCo@CNTs-60 and FeCo@CNTs-80, respectively.

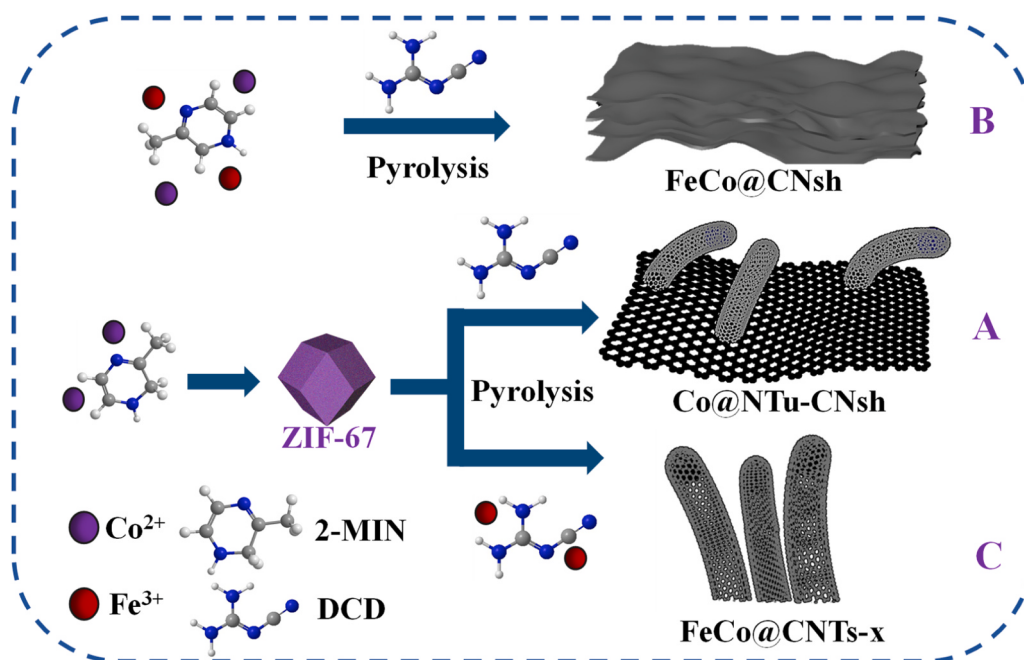


Fig. 1. Schematic diagram for preparing catalyst.

## 2.6. Characterization and measurements

The morphology of the prepared catalysts was observed by scanning electron microscopy (SEM, Thermo scientific Apreo 2 C) and transmission electron microscopy (TEM, TFEI TF20). The elemental composition was done by energy-dispersive spectroscopy (EDS, Super-X), the crystal structure and the physical phase of the catalysts were observed by X-ray power diffraction (XRD, Bruker D8 Advance), and the valence composition of the elements was analyzed by X-ray photoelectron spectroscopy (XPS, Thermo Scientific K-Alpha). The Raman spectroscopy (Raman, Horiba Scientific LabRAM HR Evolution) was used for analysis of carbon material composition and graphitization. The Brunauer-Emmett-Teller (BET) was done on a Micromeritics Tristar 3000.

All electrochemical measurements of catalysts were measured at an electrochemical station (AutoLabPGSTAT30/FRA) using a three-electrode system. The auxiliary electrode was a Pt foil, the reference electrode was Ag/AgCl electrode equipped with saturated KCl solution,

and the working electrode was a glass carbon coated with catalyst ink. The catalyst ink was prepared by mixing 5 mg of catalyst powder, 950  $\mu$ l of anhydrous ethanol and 50  $\mu$ l of Nafion solution and sonicating for 1 h. Then 20  $\mu$ l of ink was transferred to the surface of the glassy carbon electrode (0.071  $\text{cm}^2$ ) and then dried at room temperature to obtain the working electrode with a catalyst loading of 1.4  $\text{mg}\cdot\text{cm}^{-2}$ . For comparison, two benchmark working electrodes loaded with Pt/C and IrO<sub>2</sub> (0.7  $\text{mg}\cdot\text{cm}^{-2}$ ) were also prepared using the similar procedure. The potential obtained from the test was converted into the potential of the reversible hydrogen electrode (RHE) according to the equation  $E$  (vs RHE) =  $E$  vs (Ag/AgCl) +  $E$  (Ag/AgCl) + 0.059 pH.

Contributions of iron and cobalt to ORR and OER activity were investigated by using the first-principles calculations through using Vienna ab initio simulation package based on DFT. Detailed calculation process was shown in Supporting Information.

All cell performance measurements were performed on a Neware battery testing system (CT-4008-5V50 mA-164, China). The air electrode was obtained by applying 50  $\mu$ l of catalyst ink uniformly on carbon

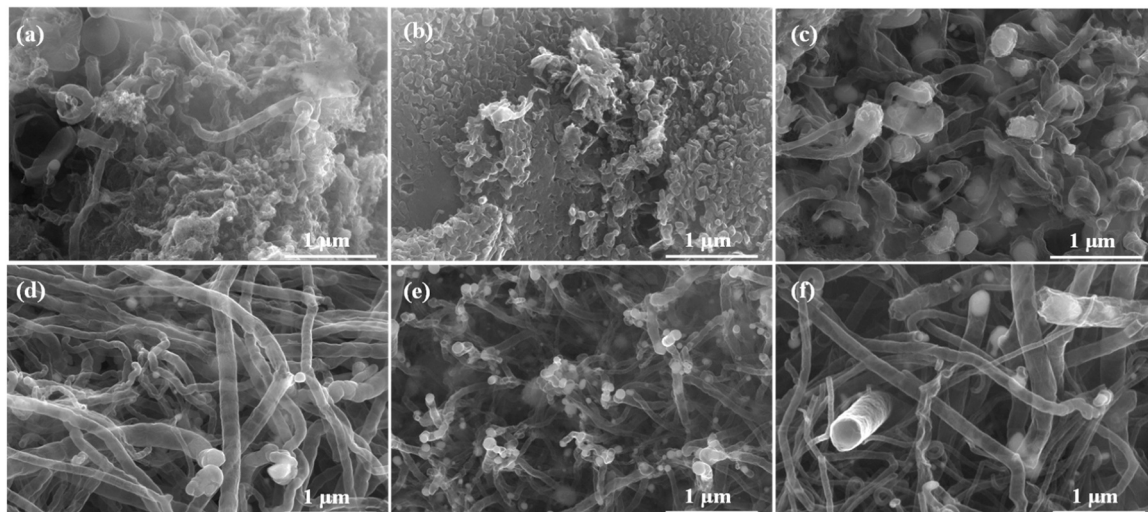
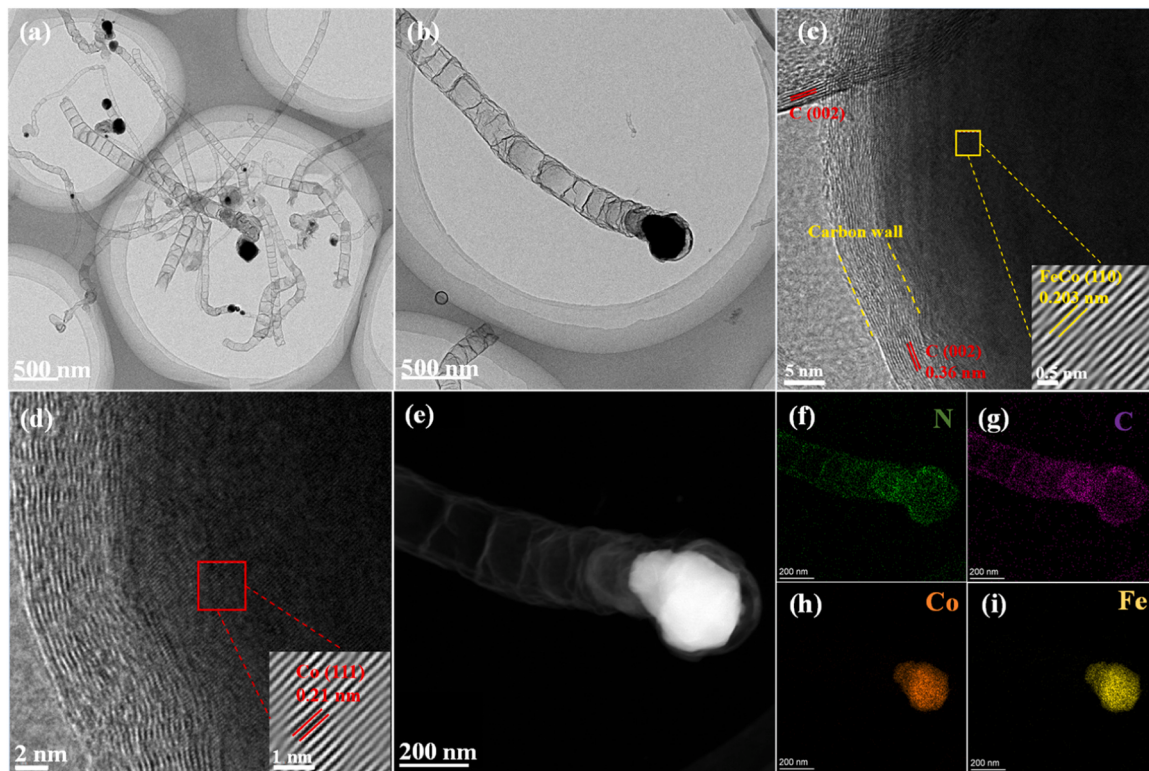


Fig. 2. SEM images of Co@NTu-CNsh (a), FeCo@CNsh (b), FeCo@CNTs-20 (c), FeCo@CNTs-40 (d), FeCo@CNTs-60 (e), FeCo@CNTs-80 (f).



**Fig. 3.** TEM and HRTEM images of (a)-(d) FeCo@CNTs-60 and SEM image for EDS measurement (e) and corresponding elemental mapping images for N (f), C (g), Co (h) and Fe (i) of FeCo@CNTs-60.

cloth and then dried at room temperature with a catalyst loading of 2.50 mg·cm<sup>-2</sup>. Pt/C and Pt/C+IrO<sub>2</sub> (mass ratio 1:1) air electrodes with a loading of 1.25 mg·cm<sup>-2</sup> were also prepared in the same way. Polished zinc plates were used as the anode and 6 M KOH aqueous solution was used as the electrolyte. It is worth noting that the electrolyte used in the cyclic charging and discharging process is 6 M KOH + 0.5 M (CH<sub>3</sub>COO)<sub>2</sub>Zn. All electrochemical tests were performed at ambient temperature.

### 3. Results and discussion

The catalyst preparation process is shown in Fig. 1. The synthesis of catalyst Co@NTu-CNsh is shown in process A, where pyrolysis of the mixture of ZIF-67 and DCD to produce sheet-like carbon and tubular carbon. From Fig. 2a we can observe that the Co@NTu-CNsh sample contains carbon nanotubes wrapped with metallic cobalt and also contains stacked carbon nanosheets. During the pyrolysis at different temperature, the structural rearrangement of DCD leads to the formation of carbon nanosheets. Besides that, metallic Co nanoparticles, produced via the reduction of Co in ZIF-67 under N<sub>2</sub> atmosphere, act as the catalytic centers of carbon nanotubes (CNTs) where the nitrogen-doped carbon nanosheets and carbon nanoparticles formed by the decomposition of DCD and ZIF-67 grow toward the metallic Co, and finally form CNTs encapsulated with Co [26,30]. In process B, simultaneous reaction of iron nitrate and cobalt nitrate with 2-methylimidazole to form Fe/Co-MOF, followed by the addition of DCD and pyrolysis treatment to obtain FeCo@CNsh. Fig. 2b shows that the catalyst FeCo@CNsh shows an overall flower-like structure, resulting from the irregular stacking and interlacing of carbon nanosheets. It is possible that the introduction of Fe<sup>3+</sup> disrupts the molding of ZIF-67, indicating that ZIF-67 is an indispensable precursor for the formation of CNTs. The FeCo@CNTs-x was obtained by pyrolysis in ZIF-67 with the addition of DCD and FeCl<sub>3</sub>·6 H<sub>2</sub>O, as revealed as the process C. We can observe that the morphology of catalysts FeCo@CNTs-x (Fig. 2c-f) is almost the intertwined carbon

nanotubes wrapped with metal nanoparticles. Because the introduced Fe<sup>3+</sup> can also be reduced to metallic iron to provide metal nuclei for the growth of CNTs, more CNTs are formed and almost no agglomerated stacking appears compared to Co@NTu-CNsh. It can also be observed that FeCo@CNTs-20, FeCo@CNTs-40 and FeCo@CNTs-80 have different diameters of CNTs and the CNTs are intertwined with each other, covering the space in the picture with fewer voids. In contrast, the CNTs of FeCo@CNTs-60 exhibits relatively uniform and small tube diameters, and multiple CNTs are entangled to form a cluster, leaving a larger gap between each cluster (Fig. 2e and Figure S1a).

The microstructure of FeCo@CNTs-60 was further observed by HRTEM (Fig. 3a and b), showing a hollow bamboo-like CNT. The bamboo-like structure formation can be attributed to nitrogen doping, which can promote oxygen adsorption and reduce the overpotential of the ORR [31–33]. The average tube length of the CNTs is ca. 2840 nm and the average tube diameter is about 88.90 nm. The longer hollow CNT structure can increase the active area of the catalyst and provide a channel for rapid electron transfer [34]. From Figure S1b and Figure S1c, it can be observed that the graphite layers in the CNT wall are interspersed with each other, which will expose more edges compared to the graphite layers in the parallel CNT direction, bringing a larger reaction area and enhanced catalytic performance [35]. The graphene (002) with a lattice spacing of 0.36 nm can be observed in Fig. 3c, and the number of graphene layers is about 16. The structure of multiple graphene layers wrapped with metal can avoid metal agglomeration as well as erosion by electrolyte and enhance the stability of the catalyst. Observing the metal nanoparticles within the CNT vertices (Fig. 3c), 0.203 nm corresponds to the (110) face of FeCo [36, 37], which indicates that metallic cobalt and metallic iron form an alloy, and the (111) face of Co with a lattice spacing of 0.21 nm is also observed from Fig. 3d [38,39]. According to the mapping SEM results (Fig. 3f-i), it can be observed that C and N are uniformly distributed on the CNTs, while Co and Fe nanoparticles are concentrated at the top of the CNTs and no separate metal nanoparticle is observed, which further

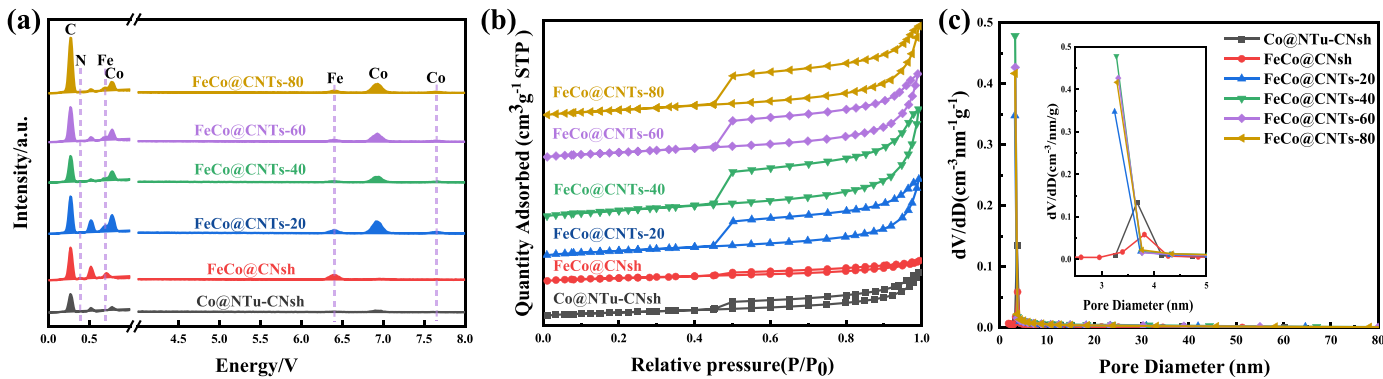


Fig. 4. EDS spectrum (a), Nitrogen adsorption–desorption isotherms (b) and pore size distributions (inset: partial enlargement) (c) of all catalysts.

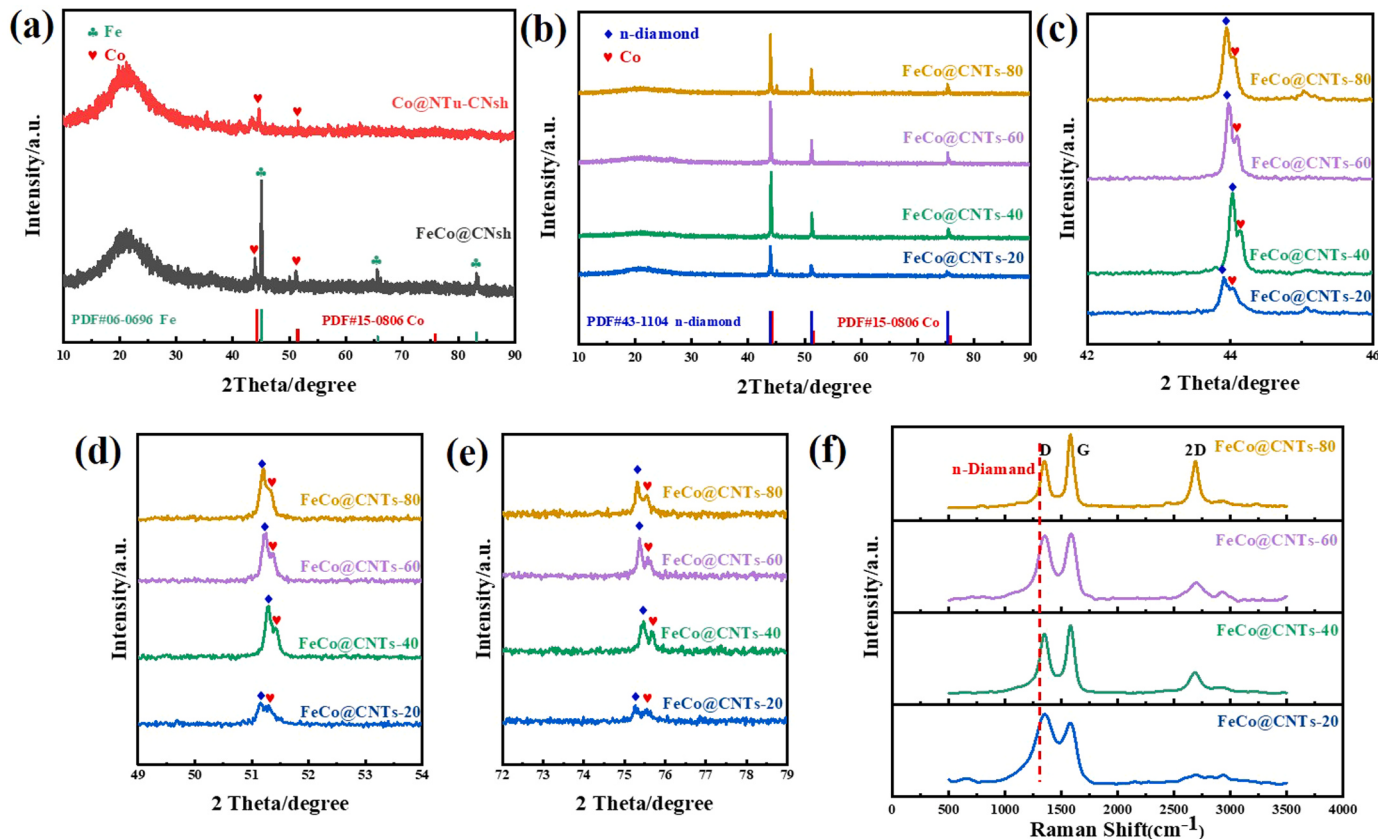


Fig. 5. XRD patterns of Co@NTu-CNsh and FeCo@CNsh (a) XRD patterns (b), local magnification(c-e) and Raman spectra (f) of FeCo@CNTs-x.

indicates the alloying behavior between Fe and Co as well as the role of Fe and Co as the nuclei of CNT growth. For N-doped CNTs, Fe-Co co-doping can reduce the overpotential during catalysis, making the electrocatalytic reaction easier and improving the electrocatalytic activity. The EDS shown in Fig. 4a demonstrates the elemental composition of the catalysts. The EDS spectra of both FeCo@CNsh and FeCo@CNTs-x reveal the presence of C, N, Fe and Co, while Co@NTu-CNsh has no peaks corresponding to Fe elements. This indicates that Fe was successfully doped into the samples FeCo@CNsh and FeCo@CNTs-x.

The  $N_2$  adsorption and desorption isotherms of the samples are shown in Fig. 4b. All the samples showed typical type IV adsorption isotherms accompanied with obvious hysteresis, indicating the presence of abundant mesopores in the catalysts. The specific surface areas of Co@NTu-CNsh, FeCo@CNsh, FeCo@CNTs-20, FeCo@CNTs-40, FeCo@CNTs-60 and FeCo@CNTs-80 are 72, 81, 120, 163, 134 and

$146\text{ m}^2\text{ g}^{-1}$ , respectively, according to the BET multipoint method. The pore size distribution curves are shown in Fig. 4c, where 3–4 nm micropores predominate, further indicating that the samples are mesoporous materials. Among them, Co@NTu-CNsh and FeCo@CNsh contain some mesopores and macropores because of the presence of carbon nanosheet structures. The average pore sizes of Co@NTu-CNsh, FeCo@CNsh, FeCo@CNTs-20, FeCo@CNTs-40, FeCo@CNTs-60 and FeCo@CNTs-80 are 5.9, 7.9, 5.7, 6.1, 5.9 and 5.7 nm, respectively. The carbon nanotube structure of the catalyst FeCo@CNTs-x has a high specific surface area and a high proportion of micropores, which have the ability to expose more active sites and facilitate the rapid transport of oxygen and ions for the oxygen reduction process [40,41].

The XRD test results are shown in Fig. 5a and b. All samples have a distinct broader diffraction peak at  $21.5^\circ$ , which is attributed to the (002) plane of graphitic carbon [42]. Compared to Co@NTu-CNsh and FeCo@CNsh involving in Co (111) and (200) planes, FeCo@CNTs-x has

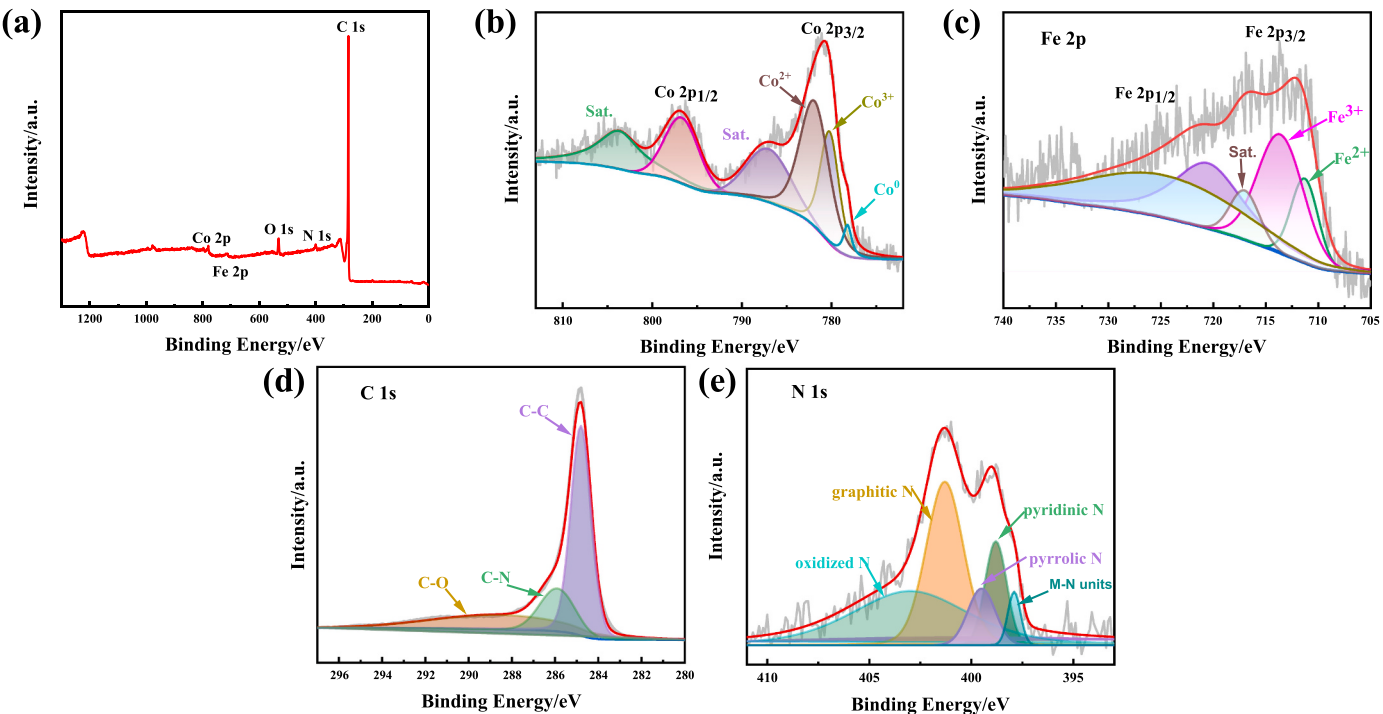


Fig. 6. XPS survey scan (a) and high-resolution Co 2p (b), Fe 2p (c), C 1s (d) and N 1s (e) spectra of FeCo@CNTs-60.

an extra (220) plane of Co. The diffraction peaks of FeCo@CNsh at 45.0, 65.6 and 83.2 correspond to the (110), (200) and (211) faces of Fe (PDF#06-0696), showing the presence of Fe in the FeCo@CNsh as demonstrated in EDS data. The XRD of FeCo@CNTs-x is shown in Fig. 5b–e. Because the FeCo@CNTs-x samples were synthesized in the same way and all have carbon nanotube structures, the diffraction peaks of the FeCo@CNTs-x series catalysts are approximately in the same position. We found three unique peaks at 43.9, 51.3 and 75.4 in FeCo@CNTs-x, which correspond to the (111), (200) and (220) crystal planes of new diamond (n-diamond, PDF#43-1104). The n-diamond is a new carbon allotrope with a face-centered cubic structure and better electrical conductivity than graphite, and its (200) peak is one of the characteristics that distinguishes it from ordinary diamond [43–46]. The presence of n-diamond may be due to the formation of CNTs catalyzed by iron at high temperatures [32]. In order to further analyze the n-diamond signal of FeCo@CNTs-x in XRD, we performed Raman spectra on the sample (Fig. 5f). Based on the typical D band peak of n-diamond at around  $1332\text{ cm}^{-1}$  and CNTs at about  $1355\text{ cm}^{-1}$  [47–49], the D band peak at  $1349\text{ cm}^{-1}$  of the FeCo@CNTs-x is shifted downward to the left by  $6\text{ cm}^{-1}$  compared with CNTs. From the Fe catalyzed conversion of CNTs to n-diamond at high temperatures, it can be concluded that the production of n-diamond leads to an increase in  $\text{sp}^3$  bonding, causing a leftward shift of the D-band peak [46]. This indicates the presence of n-diamond in the sample, but the yield is small and influenced by the D band amorphous carbon. The G band at  $1581\text{ cm}^{-1}$  is associated with graphitization of carbon, while the overtones (2D) peak at  $2690\text{ cm}^{-1}$  indicates a multilayer structure of graphite [44,50,51].

XPS measurements were performed on FeCo@CNTs-60 to further analyze its elemental composition and chemical valence states. As shown in Fig. 6a, the presence of C, N, Fe and Co indicates that the expected doping is successful. 780.7 and 797.1 eV of the Co 2p XPS spectra are Co 2p<sub>3/2</sub> and Co 2p<sub>1/2</sub>, respectively, while their satellite peaks at 787.3 and 803.8 eV. Co 2p<sub>3/2</sub> can be decomposed into Co<sup>3+</sup> (780.3 eV), Co<sup>2+</sup> (782.1 eV) and Co<sup>0</sup> (778.2 eV) peaks. The high valence of Co<sup>2+</sup> and Co<sup>3+</sup> proves the formation of the Co-N<sub>x</sub> reactive group [15, 52]. The Fe 2p<sub>1/2</sub> orbital decomposes into two peaks of 726.9 eV and 720.8 eV. Similarly, Fe 2p<sub>3/2</sub> is divided into Fe<sup>3+</sup> (713.8 eV) and Fe<sup>2+</sup>

(711.4 eV), where Fe<sup>3+</sup> is associated with the formation of FeN reactive groups [53]. The middle of Fe 2p<sub>1/2</sub> and Fe 2p<sub>3/2</sub> are satellite peaks. The C 1s spectra are shown in Fig. 6d. The C-C and C-O bonds are 284.8 eV and 288.5 eV, respectively, and the C-N bond located at 285.9 eV indicates the successful doping of N into the carbon nanotube backbone [54]. The N 1s spectra can be decomposed into five peaks of M-Nx (397.9 eV), pyridinic N (398.8 eV), pyrrolic N (399.5 eV), graphite N (401.3 eV) and oxidized N (403.0 eV). Among them, M-Nx, pyridine N and graphite N play a significant role in enhancing the ORR reaction, while pyrrolic N and oxidized N are less effective in improving the electrochemical performance [55,56].

To evaluate the ORR performance of the catalysts, we performed ORR tests in the full pH range (0.1 M KOH, 0.1 M HClO<sub>4</sub> and 1 M KCl+4 M NH<sub>4</sub>Cl). The cyclic voltammetric (CV) of the catalyst is shown in Figure S2. The CV curves measured in O<sub>2</sub>-saturated atmosphere exhibit a clear oxygen reduction peak compared to those in N<sub>2</sub>-saturated atmosphere, which indicates the good ORR performance of the prepared catalysts. Linear sweep voltammetry (LSV) was also used to further compare the electrocatalytic activity of the catalysts. The LSV curves of the catalysts and Pt/C at 1600 pm are shown in Fig. 7a–c, and the corresponding specific values related to the ORR onset potential ( $E_{\text{onset}}$ ), half-slope potential ( $E_{1/2}$ ) and limiting diffusion current ( $j$ ) are shown in Fig. 7d–f. Results indicate that the catalysts FeCo@CNTs-x are superior to Co@NTu-CNsh and FeCo@CNsh in the full pH range for both  $E_{\text{onset}}$  and  $E_{1/2}$ . This is due to the structural advantage of metal nanoparticles-encapsulated CNTs and the synergistic effect of Fe and Co. Meanwhile, the ORR performance of the samples shows an enhanced trend with the increase of x in FeCo@CNTs-x. The corresponding catalyst at x = 60 achieves the best ORR performance, while the electrocatalytic activity decreases when x increases to 80. Result indicates the great effect of the structural regulation obtained by adjusting the Fe and Co molar ratio on the ORR performance. The increase in the number of CNTs and the entanglement of CNTs with each other will lead to space congestion, difficulty in material transfer and low efficiency in active site utilization, which eventually causes a decrease in ORR activity [15,54]. In 0.1 M KOH solution (Fig. 7a and c), FeCo@CNTs-40 ( $E_{\text{onset}} = 1.05\text{ V}$ ,  $E_{1/2} = 0.95\text{ V}$ ) and FeCo@CNTs-60 ( $E_{\text{onset}} = 1.05\text{ V}$ ,  $E_{1/2} = 0.95\text{ V}$ ) have

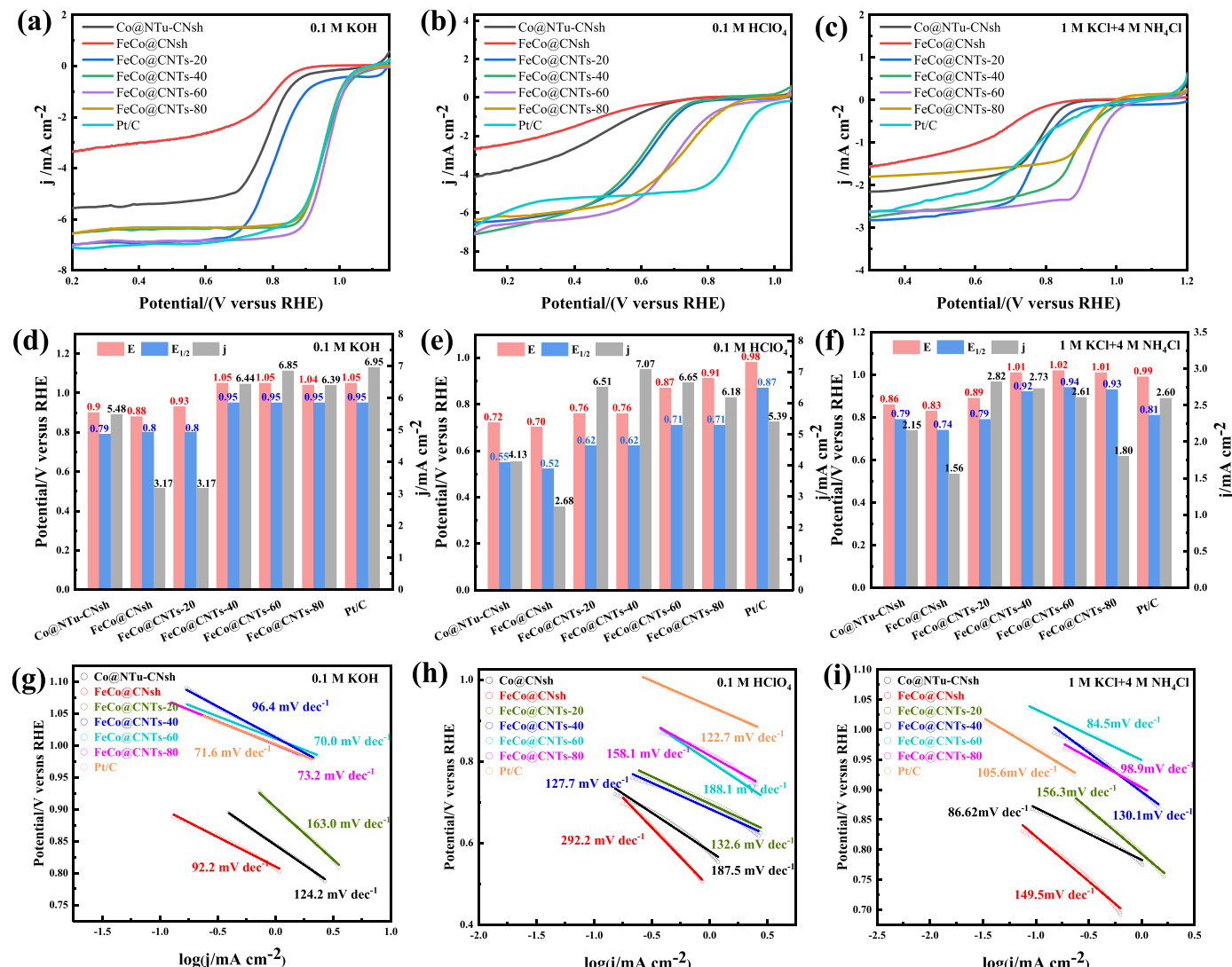


**Fig. 7.** LSV curves of all catalysts in  $\text{O}_2$ -saturated 0.1 M KOH (a), 0.1 M  $\text{HClO}_4$  (b) and 4 M  $\text{NH}_4\text{Cl} + 1 \text{ M KCl}$  (c) at  $5 \text{ mV s}^{-1}$  and 1600 rpm. Corresponding onset potential, half-wave potential and limiting diffusion current density (d-f). Tafel plots for all catalysts in  $\text{O}_2$ -saturated 0.1 M KOH (g), 0.1 M  $\text{HClO}_4$  (h) and 4 M  $\text{NH}_4\text{Cl} + 1 \text{ M KCl}$  (i).

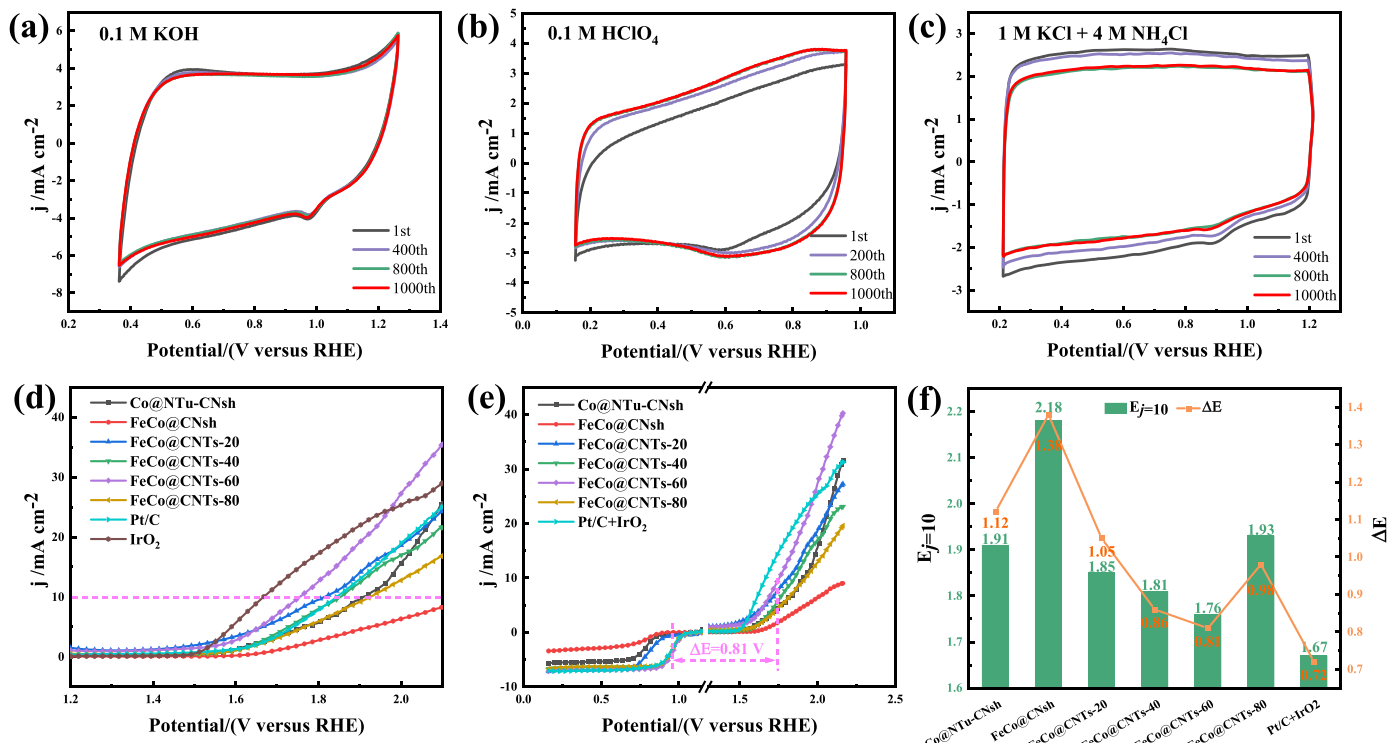
comparable  $E_{onset}$  and  $E_{1/2}$  to Pt/C ( $E_{onset} = 1.05 \text{ V}$ ,  $E_{1/2} = 0.95 \text{ V}$ ). In 0.1 M  $\text{HClO}_4$  solution (Fig. 7b and e), FeCo@CNTs-60 and FeCo@CNTs-80 have the best ORR activity among the prepared catalysts, but still lower than Pt/C. This is a common challenge that most non-noble metal-containing carbon-based catalysts display a poor ORR activity in acid media [57]. In 1 M KCl+ 4 M  $\text{NH}_4\text{Cl}$  solution, FeCo@CNTs-40 ( $E_{onset} = 1.01 \text{ V}$ ,  $E_{1/2} = 0.92 \text{ V}$ ), FeCo@CNTs-60 ( $E_{onset} = 1.02 \text{ V}$ ,  $E_{1/2} = 0.94 \text{ V}$ ) and FeCo@CNTs-80 ( $E_{onset} = 1.01 \text{ V}$ ,  $E_{1/2} = 0.93 \text{ V}$ ) all have higher  $E_{onset}$  and  $E_{1/2}$  than Pt ( $E_{onset} = 0.99 \text{ V}$ ,  $E_{1/2} = 0.81 \text{ V}$ ). Among them, FeCo@CNTs-60 has the best ORR performance.

Fig. 7j and i show the Tafel curves derived from LSVs at 1600 pm in alkaline, acidic and neutral conditions. We can observe that in alkaline and neutral media the FeCo@CNTs-60 ( $70.0 \text{ mV dec}^{-1}$  and  $84.5 \text{ mV dec}^{-1}$ ) catalyst has a lower Tafel slope than the other catalysts and Pt/C ( $71.6 \text{ mV dec}^{-1}$  and  $105.6 \text{ mV dec}^{-1}$ ). This indicates that FeCo@CNTs-60 has a faster ORR kinetics. In acidic solution, the Tafel slope of FeCo@CNTs-x is lower than that of Co@NTu-CNsh and FeCo@CNsh, which again indicates that the rational design for the microstructure of the samples, and the molar ratio of Fe and Co can effectively improve the electrocatalyst performance.

In order to evaluate the ORR activity stability of the catalysts, we conducted 1000 consecutive cycling scans of the FeCo@CNTs-60 as a

typical sample in alkaline, acidic and neutral media. In 0.1 M KOH solution shown in Fig. 8a, the curves of the catalysts almost completely overlapped after 1000 times of CV cycles, which indicated that FeCo@CNTs-60 has good electrocatalytic stability in alkaline solution. In acidic electrolyte (Fig. 8b), the CV test showed a positive potential shift and capacitance increase in the early stage, and then stabilized. Considering that Fe and Co are not completely encapsulated within the CNTs under high-temperature pyrolysis, some free Fe and Co species will still be present. The long time testing under acidic electrolyte leads to the removal of these free and inactive metal species, exposing the electrochemically active sites and thus resulting in a positive shift in potential and an increase in capacitance [58]. In the neutral electrolyte (Fig. 8c), we can observe a negative potential shift and a decrease in capacitance as the number of test cycles increases. This may be due to the fact that the 4 M  $\text{NH}_4\text{Cl} + 1 \text{ M KCl}$  electrolyte used is a quasi-neutral concentrated salt solution and the electrolyte is directly exposed to air. As the cycle progresses, a small amount of salt precipitates and adheres to the surface of the electrode, covering the active sites, and ultimately resulting in a negative potential shift and capacitance decrease.

Under 200 cycles of testing (Figure S3), the  $E_{onset}$  remained unchanged ( $E_{onset} = 0.77 \text{ V}$ ). The current produced a 16 % shift, which was related to that excessive catalyst loading may cause a small amount of



**Fig. 8.** CVs for 1000 consecutive sweeps in O<sub>2</sub>-saturated 0.1 M KOH (a), 0.1 M HClO<sub>4</sub> (b) and 4 M NH<sub>4</sub>Cl + 1 M KCl (c) solution at 100 mV·s<sup>-1</sup>. OER curves in O<sub>2</sub>-saturated 0.1 M KOH solution at 5 mV·s<sup>-1</sup> and 1600 rpm (d). Overall polarization curves for the ORR and OER (e). Corresponding  $E_{j=10}$  and the  $E_{1/2}$  (f).

catalyst shedding during the test. SEM of the sample after the 200 cycles of testing shown in Figure S4 indicates the presence of a large number of bamboo-like CNTs. XRD and XPS data (Figure S5) of the sample after the 200 cycles basically remain the same characteristics as those of the freshly prepared sample. Results indicate that the catalyst has good stability after repeated testing.

To explore the possible application of the samples to rechargeable Zn-air battery, we tested their OER performance in alkaline electrolyte. Fig. 8d shows the OER activity plots at 1600 rpm in O<sub>2</sub>-saturated 0.1 M KOH. As in the ORR case, FeCo@CNTs-60 ( $E_{j=10} = 1.76$  V) exhibits better OER activity than the other catalysts and Pt/C at a current density of 10 mA, slightly lower than IrO<sub>2</sub> ( $E_{j=10} = 1.67$  V). However, at high current densities (when the  $j$  is greater than 24.6  $\text{mA cm}^{-2}$ ), FeCo@CNTs-60 outperforms IrO<sub>2</sub> in OER performance. The potential difference between  $E_{j=10}$  for OER and  $E_{1/2}$  for ORR ( $\Delta E = E_{j=10} - E_{1/2}$ ) is an important factor in assessing the bifunctional activity, and a small value of  $\Delta E$  approximately indicates a better bifunctional catalytic effect of the catalyst [59]. As shown in Fig. 8e for the  $\Delta E$  of the prepared catalysts, FeCo@CNTs-60 exhibited a low  $\Delta E$  value of 0.81 V slightly higher than Pt/C+IrO<sub>2</sub> by 90 mV. This indicates that the FeCo@CNTs-60 is the most suitable bifunctional catalyst among the samples. In addition, we used the method of Fang et al. [60] to remove the metals doped in the CNTs (see Supporting Information for the specific method) in order to investigate the role of the doped FeCo nanoparticles in the ORR/OER activity. Figure S6 shows that from HRTEM micrographs of the sample removed metal, no metal particles were observed in the CNTs. Electrochemical tests are shown in Figure S7, where we can find that the metal-removed CNTs exhibit poor ORR ( $E_{\text{onset}} = 0.77$  V) and OER ( $E_{j=10} = 1.88$  V) catalytic activities. This suggests that doping metal iron and cobalt can effectively improve the ORR/OER activity.

To further investigate the synergistic of Fe and Co, we built a relevant theoretical model for the sample FeCo@CNTs-60 (Fig. 9a) and performed corresponding calculations of Co-CNT and CoFe-CNT using DFT (See Supporting Information for relevant calculation details), and ORR/OER intermediates models are shown in Fig. 9d. As indicated in Fig. 9b,

ORR consists of four basic processes: (1)  $^* + \text{O}_2 + \text{H}_2\text{O} + \text{e}^- \rightarrow \text{OOH}^* + \text{OH}^-$ , (2)  $\text{OOH}^* + \text{e}^- \rightarrow \text{O}^* + \text{OH}^-$ , (3)  $\text{O}^* + \text{H}_2\text{O} + \text{e}^- \rightarrow \text{OH}^* + \text{OH}^-$  and (4)  $\text{OH}^* + \text{e}^- \rightarrow \text{OH}^- + ^*$  [61]. Among the four steps, the one with the smallest Gibbs free energy ( $\Delta G$ ) is the decision step, and the smaller change of  $\Delta G$  reveals the stronger catalytic activity of ORR [62]. The first reaction process is the decision step of Co-CNT and CoFe-CNT, and the  $\Delta G$  is 1.07 eV and 0.91 eV, respectively, which indicates that bimetallic CoFe doping contributes to the enhancement of ORR activity. OER is the reverse process of ORR with the opposite basic reaction steps. It can be observed from Fig. 9c that the  $\Delta G$  of 0.79 eV for CoFe-CNT is lower than that of 0.89 eV for Co-CNT, which indicates that the co-doping of metal Co and Fe reduces the OER reaction energy barrier and strengthens the OER activity. Therefore, the theoretical calculations indicate that the metal Fe and Co systems exhibit a good synergistic effect on the improvement of the ORR/OER bifunctional performance. Bader charge analysis (Fig. 9d) shows that the transferred charges on CoFe-CNT and OH<sup>\*</sup>CoFe-CNT are larger than those on Co-MOF and OH<sup>\*</sup>@Co-CNT, indicating that the interaction between bimetallic CoFe and CNT is stronger than that of single-metal Co. Fig. 9d also shows that CoFe-CNT can accelerate the reductive release of intermediate OH<sup>\*</sup>, reducing the reaction barrier and promoting the ORR/OER process. As shown in Fig. 9e and f, the d-band center of CoFe-CNT is positively shifted as compared to Co-CNT, suggesting a stronger adsorption of intermediates by CoFe-CNT. This is one of the powerful reasons for the synergistic action of the bimetallic Co and Fe to increase the electrocatalytic activity.

Electroactivity of the samples was further investigated in conventional home-made zinc-air batteries to verify their effectiveness in practical applications. Fig. 10a shows the discharge polarization curves and power density plots for the catalysts and Pt/C. The FeCo@CNTs-60 delivers a peak power density of 268.3  $\text{mW cm}^{-2}$  corresponding to a current density of 398.0  $\text{mA cm}^{-2}$ , which is higher than other catalysts and Pt/C (200.6  $\text{mW cm}^{-2}$ ). Fig. 10b shows the step discharge curves for FeCo@CNTs-60 and Pt/C. We can observe that at low current densities of 10 and 20  $\text{mA cm}^{-2}$  the voltage plateau of FeCo@CNTs-60 is slightly

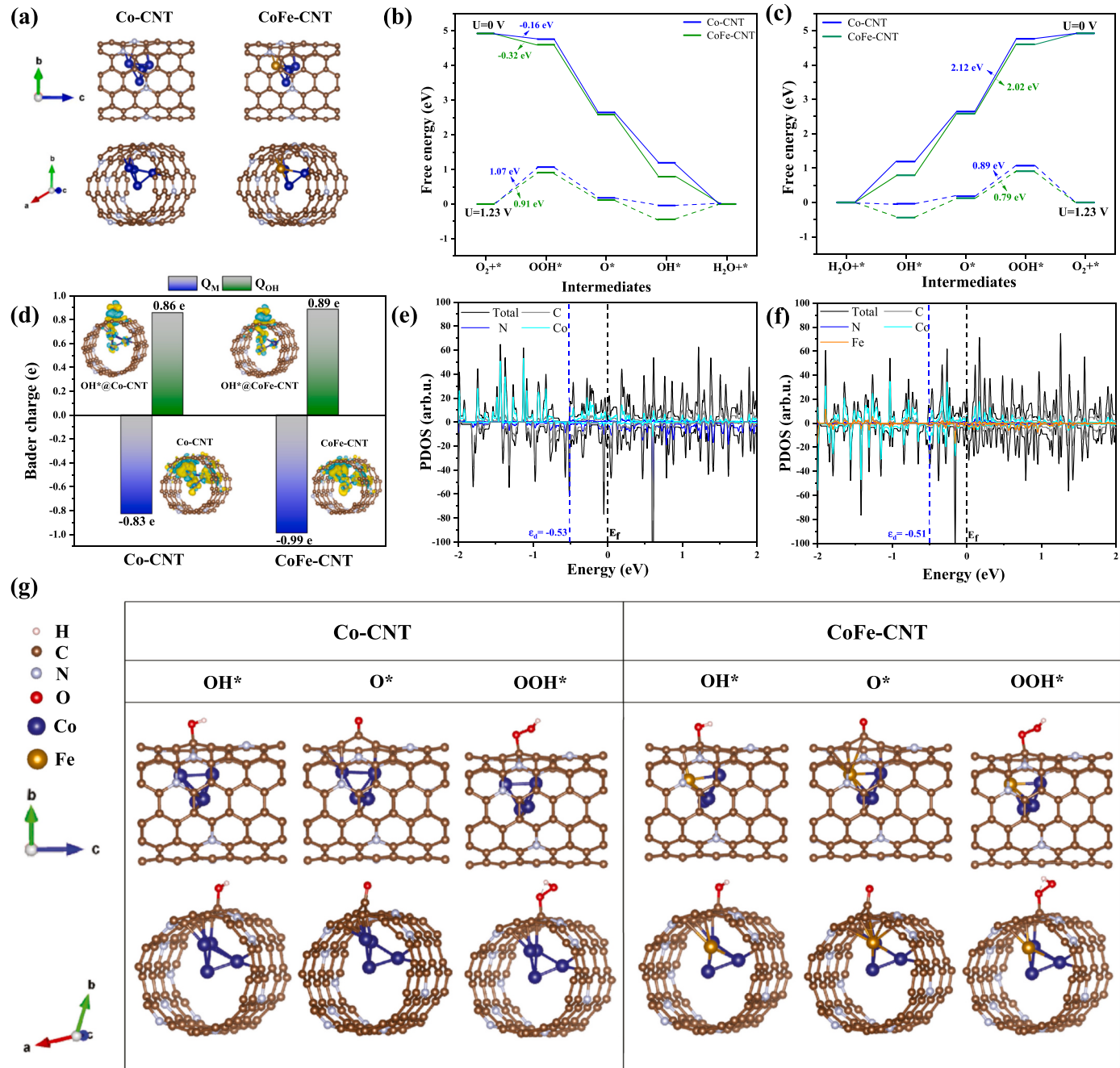


**Fig. 9.** Theoretical modeling of Co-CNT and CoFe-CNT (a). ORR (b) and OER(c) free energy diagrams for Co-CNT and CoFe-CNT. Bader charge analysis of  $OH^*$  adsorbed on Co-CNT and CoFe-CNT (d). Projected density of states (PDOS) analysis of Co-CNT (e) and CoFe-CNT (f). Stabilized adsorption configurations of ORR/OER intermediates (d).

lower than that of Pt/C. When the current density rises to  $50 \text{ mA} \cdot \text{cm}^{-2}$ , the voltage of FeCo@CNTs-60 is the same as that of Pt/C. When the current density reaches  $100 \text{ mA} \cdot \text{cm}^{-2}$ , the plateau of FeCo@CNTs-60 exceeds that of Pt/C. This indicates that FeCo@CNTs-60 performs better at high current densities. Further verification on the stability of FeCo@CNTs-60 was obtained from the constant current discharge (Fig. 10c). FeCo@CNTs-60 was discharged at a current density of  $50 \text{ mA} \cdot \text{cm}^{-2}$  for up to 70 h at constant current, during which the voltage plateau was stable and the cell stopped at 73 h due to corrosion perforation of the anode zinc sheet. The cell starts at  $1.24 \text{ V}$  and after 70 h of the stable operation, the cell voltage remains at  $1.13 \text{ V}$  and only decreases by 110 mV. After normalizing the weight of zinc sheet, the specific capacity of the battery with FeCo@CNTs-60 is  $802.1 \text{ mA} \cdot \text{h} \cdot \text{kg}^{-1}$ ,

approaching the theoretical capacity of  $820 \text{ mA} \cdot \text{h} \cdot \text{kg}^{-1}$  for Zn-air battery [63].

In view of the bifunctional characteristics of the FeCo@CNTs-60 for ORR/OER, its actual charge-discharge performance tests were conducted and the results are shown in Fig. 10d and e. Each charging/discharging cycle lasts for 30 min, including 10 min of charging, 10 min of discharging and 5 min of rest between charging and discharging. In the cycle test at  $5 \text{ mA} \cdot \text{cm}^{-2}$  (Fig. 10d), FeCo@CNTs-60 has a voltage difference of  $0.80 \text{ V}$  at the beginning of the cycle and an energy efficiency (ratio of discharge voltage to charge voltage) of 60.0 %. Besides displaying a higher charge voltage ( $2.04 \text{ V}$ ) in the initial 30 h cycles, Pt/C+IrO<sub>2</sub> delivers lower discharge voltage and energy efficiency than FeCo@CNTs-60. After 90 h charge-discharge cycles, compared with the

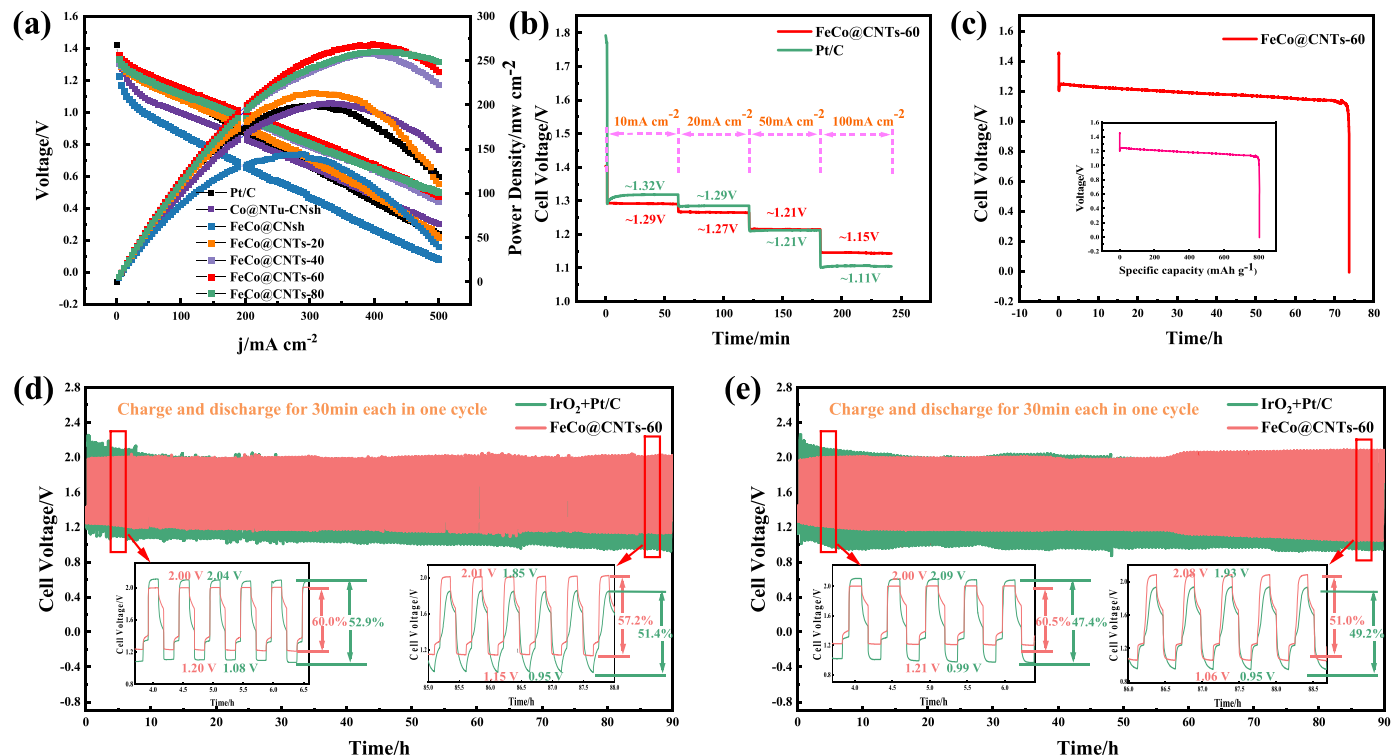


**Fig. 10.** Polarization and power density curves of Zn-air batteries in 6 M KOH electrolyte for all catalysts and Pt/C (a). Step discharge of Zn-air batteries with FeCo@CNTs-60 and Pt/C at different current densities (b). Constant current discharge curves for Zn-air batteries with FeCo@CNTs-60 at 50 mA·cm<sup>-2</sup> (inset: specific capacity of FeCo@CNTs-60) (c). Discharge - charge cycling curves of FeCo@CNTs-60 and Pt/C at 5 mA·cm<sup>-2</sup> (d) and 10 mA·cm<sup>-2</sup> (e).

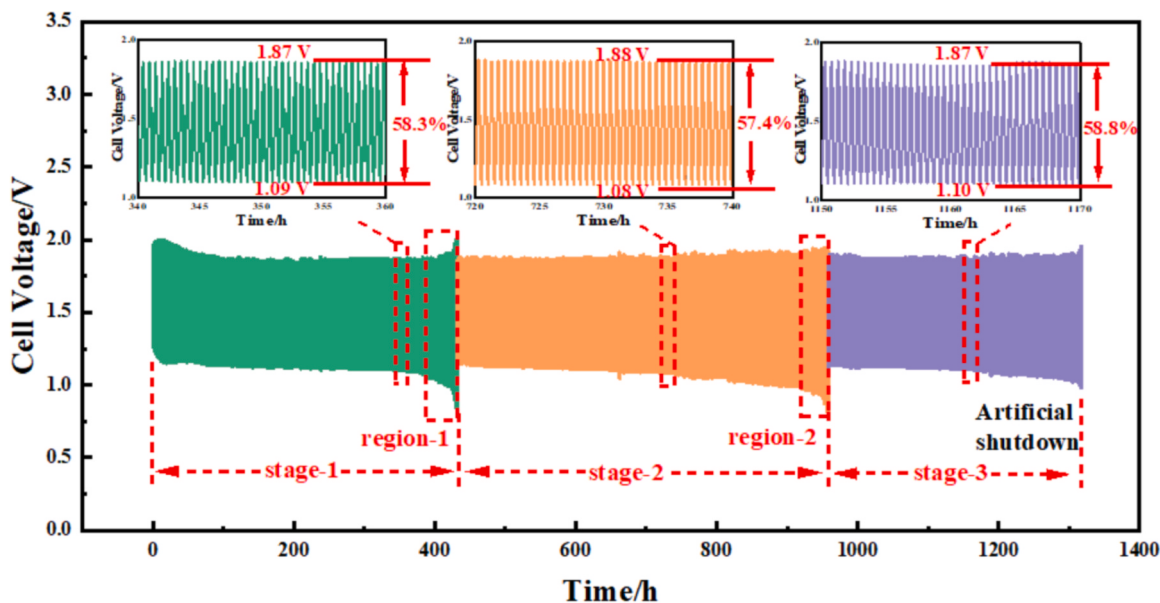


**Fig. 11.** Ultra-long-term discharge / charge cycling operation of the battery with FeCo@CNTs-60 at 5 mA·cm<sup>-2</sup>. The operation conditions of Stage-2 and Stage-3 are the same as those of Stage-1 except that Zn sheet and electrolyte are replaced with fresh ones.

obvious drop of Pt/C+IrO<sub>2</sub> charge voltage, FeCo@CNTs-60 charge voltage hardly changes. In the cycle test under 10 mA·cm<sup>-2</sup>, FeCo@CNTs-60 has a charging voltage comparable to that of Pt/C+IrO<sub>2</sub> but a larger discharging voltage. In the 90 h test, FeCo@CNTs-60 has always maintained a smaller voltage difference and greater energy efficiency than Pt/C+IrO<sub>2</sub>. Fig. 10e also shows that FeCo@CNTs-60 displays a small increase in charge voltage and a small decrease in discharge voltage at the 56th hour of testing at 10 mA·cm<sup>-2</sup>, which may

be caused by the passivation of the zinc electrode [64].

To further explore the stability of the air electrode with the catalyst FeCo@CNTs-60 during the ultra-long-term charge/discharge cycle operation of the battery, we conducted a consecutive cycle running test for over 1300 h, which was realized by replacing the anode Zn sheet and electrolyte but keeping the air electrode unchanged, as indicated in Fig. 11. It is observed from Fig. 11 that the battery has been running stably for 380 h in the first stage-1, and the charging and discharging

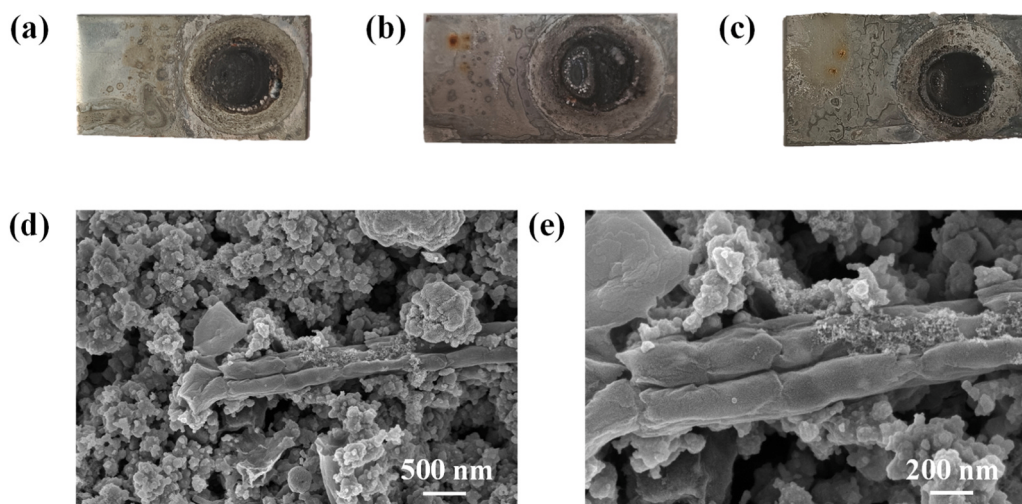


**Fig. 12.** Surface appearance of Zn sheet after Stage-1 (a), Stage-2 (b) and Stage-3 (c). SEM images (d and e) of the sample FeCo@CNTs-60 after over 1300 h of consecutive discharge/charge cycling operation.

voltage is 1.87 V and 1.09 V respectively, releasing a corresponding voltage efficiency of 58.3 %. After 380 h, the battery performance starts to decay as shown as the decline of discharge voltage and increase of charge voltage (region-1 in Fig. 11), which may be caused by the passivation of zinc electrode. Considering that the assembled cell is not a completely sealed system,  $\text{CO}_2$  in the air can enter the electrolyte and generate carbonates, resulting in a decrease in alkali concentration and subsequent difficulty in dissolving  $\text{Zn}(\text{OH})_2$ . Observing the Zn sheet (Fig. 12a), we can find a white solid attached to the surface, which may be the generated  $\text{K}_2\text{CO}_3$  or  $\text{Zn}(\text{OH})_2$ .

After the stage-1 of operation, the Zn sheet and electrolyte were replaced by fresh ones while the air electrode remained unchanged to continue with the stage-2. As shown in Fig. 11, the battery delivers almost the same discharging / charging voltages during the stage-2 as those during the stage-1. The battery still keeps the stable operation and presents high voltage efficiency, e.g., 57.4 % after 720 h of operation. This further indicates that the decay of battery performance in region-1 is caused by the Zn passivation and changes in electrolyte composition. As the battery continued to operate, the same phenomenon as that in region-1 occurred, as indicated in region-2. After we repeated the previous operation that Zn sheet and electrolyte were again replaced by fresh ones but the air electrode still remained unchanged, the battery could still restore its previous performance (stage-3). The Zn sheet taken from the battery after the stage-3 is shown in Fig. 12c, and its appearance remains basically the same. Results reveal that even though the battery undergoes ultra long-term charging/discharging cycles, the catalyst FeCo@CNTs-60 (or air electrode) still maintains surprising stability, proving the strong practicability of FeCo@CNTs-60 in rechargeable ZAB.

After the battery was cycled for more than 1300 h of charging/discharging operation, the battery was manually stopped, and the air electrode was removed and then was rinsed in pure water at 45 °C to remove the residues on the catalyst surface. Its SEM images are shown in Fig. 12d and e, which exhibits that the particles may originate from Nafion polymer and carbonate or alkali. We can observe the presence of bamboo-like carbon nanotubes, which thickening of tube diameter may be ascribed to the deposition of polymer and salts on its surface. This indicates that the catalyst morphology can be maintained better, which may contribute to the ultra-high stability of the catalyst.

#### 4. Conclusions

In conclusion, a series of nitrogen-doped CNTs loading with Fe and Co were synthesized by simple pyrolysis using Co-MOF as precursor, and

the best bifunctional catalyst FeCo@CNTs-60 was obtained by adjusting the ratio of Fe and Co. FeCo@CNTs-60 exhibits a comparable ORR performance with Pt/C in alkaline solution and significantly better catalytic performance than Pt/C in neutral solution. In addition, the rechargeable Zn-Air batteries constructed based on FeCo@CNTs-60 exhibit high stability and durability, with higher power density than Pt/C and better cyclic charge/discharge performance than Pt/C+IrO<sub>2</sub> at high current density. The excellent performance of FeCo@CNTs-60 is related to its unique structure. The bamboo-like nitrogen-doped CNTs wrapped with Fe and Co provide a channel for rapid electron transfer and also protect the Fe and Co active sites. On the other hand, the synergistic effect of Fe and Co, high content of graphitic carbon, and more active sites also enhance their ORR activity. This study provides a new idea for the synthesis of carbon materials using MOFs materials as precursors, and also provides a reference scheme for the synthesis of bifunctional catalysts doped with Fe and Co.

#### CRediT authorship contribution statement

**Can Fang:** Synthesis, Measurement and Writing-Original draft preparation. **Xiangmei Tang:** Measurement. **Qingfeng Yi:** Supervision.

#### Declaration of Competing Interest

There are no conflicts of interest to declare.

#### Data Availability

Data will be made available on request.

#### Acknowledgments

Authors sincerely thank the financial support from the National Natural Science Foundation of China (Nos. 22379042 and 21875062) and the Research and Development Planning Projects in Key Areas of Hunan Province (No. 2019GK2034).

#### Appendix A. Supporting information

Supplementary data associated with this article can be found in the online version at doi:10.1016/j.apcatb.2023.123346.

## References

[1] A. Radwan, H. Jin, B. Liu, Z. Chen, Q. Wu, X. Zhao, D. He, S. Mu, 3D-ZIF scaffold derived carbon encapsulated iron nitride as a synergistic catalyst for ORR and zinc-air battery cathodes, *Carbon* 171 (2021) 368–375.

[2] Z.-Y. Mei, S. Cai, G. Zhao, X. Zou, Y. Fu, J. Jiang, Q. An, M. Li, T. Liu, H. Guo, Boosting the ORR active and Zn-air battery performance through ameliorating the coordination environment of iron phthalocyanine, *Chem. Eng. J.* 430 (2022), 132691.

[3] M.-I. Jamesh, P. Moni, A.S. Prakash, M. Harb, ORR/OER activity and zinc-air battery performance of various kinds of graphene-based air catalysts, *Mater. Sci. Energy Technol.* 4 (2021) 1–22.

[4] K. Chen, S. Kim, R. Rajendiran, K. Prabakar, G. Li, Z. Shi, C. Jeong, J. Kang, O.L. Li, Enhancing ORR/OER active sites through lattice distortion of Fe-enriched FeNi<sub>3</sub> intermetallic nanoparticles doped N-doped carbon for high-performance rechargeable Zn-air battery, *J. Colloid Interface Sci.* 582 (2021) 977–990.

[5] W.-Z. Cheng, J.-L. Liang, H.-B. Yin, Y.-J. Wang, W.-F. Yan, J.-N. Zhang, Bifunctional iron-phthalocyanine metal-organic framework catalyst for ORR, OER and rechargeable zinc-air battery, *Rare Met.* 39 (2020) 815–823.

[6] Z.-Y. Mei, S. Cai, G. Zhao, Q. Jing, X. Sheng, J. Jiang, H. Guo, Understanding electronic configurations and coordination environment for enhanced ORR process and improved Zn-Air battery performance, *Energy Storage Mater.* 50 (2022) 12–20.

[7] Y. Feng, K. Song, W. Zhang, X. Zhou, S.J. Yoo, J.-G. Kim, S. Qiao, Y. Qi, X. Zou, Z. Chen, Efficient ORR catalysts for zinc-air battery: biomass-derived ultra-stable Co nanoparticles wrapped with graphitic layers via optimizing electron transfer, *J. Energy Chem.* 70 (2022) 211–218.

[8] Q. Niu, B. Chen, J. Guo, J. Nie, X. Guo, G. Ma, Flexible, porous, and metal-heteroatom-doped carbon nanofibers as efficient ORR electrocatalysts for Zn-air battery, *Nanomicro Lett.* 11 (2019), 8.

[9] J. Lim, J.-W. Jung, N.-Y. Kim, G.Y. Lee, H.J. Lee, Y. Lee, D.S. Choi, K.R. Yoon, Y.-H. Kim, I.-D. Kim, S.O. Kim, N<sub>2</sub>-dopant of graphene with electrochemically switchable bifunctional ORR/OER catalysis for Zn-air battery, *Energy Storage Mater.* 32 (2020) 517–524.

[10] L. Chai, L. Zhang, X. Wang, L. Xu, C. Han, T.-T. Li, Y. Hu, J. Qian, S. Huang, Bottom-up synthesis of MOF-derived hollow N-doped carbon materials for enhanced ORR performance, *Carbon* 146 (2019) 248–256.

[11] Y. Zhou, B. Tang, S. Wang, J. Long, Cu-MOF@ Co-MOF derived Co-Cu alloy nanoparticles and N atoms co-doped carbon matrix as efficient catalyst for enhanced oxygen reduction, *Int. J. Hydrogen Energy* 45 (2020) 15785–15795.

[12] F. Calle-Vallejo, J.I. Martinez, J. Rossmeisl, Density functional studies of functionalized graphitic materials with late transition metals for oxygen reduction reactions, *Phys. Chem. Chem. Phys.* 13 (2011) 15639–15643.

[13] Y. Wang, Y. Pan, L. Zhu, H. Yu, B. Duan, R. Wang, Z. Zhang, S. Qiu, Solvent-free assembly of Co/Fe-containing MOFs derived N-doped mesoporous carbon nanosheets for ORR and HER, *Carbon* 146 (2019) 671–679.

[14] X. Duan, S. Ren, N. Pan, M. Zhang, H. Zheng, MOF-derived Fe,Co@N-C bifunctional oxygen electrocatalysts for Zn-air batteries, *J. Mater. Chem. A* 8 (2020) 9355–9363.

[15] K. Sheng, Q. Yi, A.L. Chen, Y. Wang, Y. Yan, H. Nie, X. Zhou, CoNi nanoparticles supported on N-doped bifunctional hollow carbon composites as high-performance ORR/OER catalysts for rechargeable Zn-air batteries, *ACS Appl. Mater. Interfaces* 13 (2021) 45394–45405.

[16] K. Song, J. Wei, W. Dong, Z. Zou, J. Wang, Fe<sub>3</sub>O<sub>4</sub>/N-CNTs derived from hypercrosslinked carbon nanotube as efficient catalyst for ORR in both acid and alkaline electrolytes, *Int. J. Hydrogen Energy* 47 (2022) 20529–20539.

[17] T. Wang, L. Xu, C. Sun, X. Li, Y. Yan, F. Li, Synthesis of hierarchically structured Fe<sub>3</sub>C/CNTs composites in a FeNC matrix for use as efficient ORR electrocatalysts, *RSC Adv.* 13 (2023) 3835–3842.

[18] R. Jena, S. Bhattacharyya, N. Bothra, V. Kashyap, S.K. Pati, T.K. Maji, Ni<sub>x</sub>Co<sub>1-x</sub>@Ni<sub>x</sub>Co<sub>1-x</sub>O/NCNT trifunctional ORR, OER, and HER electrocatalysts and its application in a Zn-air battery, *ACS Appl. Mater. Interfaces* 15 (2023) 27893–27904.

[19] L. Yang, J. Shui, L. Du, Y. Shao, J. Liu, L. Dai, Z. Hu, Carbon-based metal-free ORR electrocatalysts for fuel cells: past, present, and future, *Adv. Mater.* 31 (2019), 1804799.

[20] A. Ajiaz, J. Masa, C. Rosler, W. Xia, P. Weide, A.J. Botz, R.A. Fischer, W. Schuhmann, M. Muhler, Co@Co<sub>3</sub>O<sub>4</sub> encapsulated in carbon nanotube-grafted nitrogen-doped carbon polyhedra as an advanced bifunctional oxygen electrode, *Angew. Chem. Int. Ed.* 55 (2016) 4087–4091.

[21] G. Xu, G.-C. Xu, J.-J. Ban, L. Zhang, H. Lin, C.-L. Qi, Z.-P. Sun, D.-Z. Jia, Cobalt and cobalt oxides N-codoped porous carbon derived from metal-organic framework as bifunctional catalyst for oxygen reduction and oxygen evolution reactions, *J. Colloid Interface Sci.* 521 (2018) 141–149.

[22] C. Xu, Z. Lin, D. Zhao, Y. Sun, Y. Zhong, J. Ning, C. Zheng, Z. Zhang, Y. Hu, Facile in situ fabrication of Co nanoparticles embedded in 3D N-enriched mesoporous carbon foam electrocatalyst with enhanced activity and stability toward oxygen reduction reaction, *J. Mater. Sci.* 54 (2019) 5412–5423.

[23] J.-K. Sun, Q. Xu, Functional materials derived from open framework templates/precursors: synthesis and applications, *Energy Environ. Sci.* 7 (2014) 2071–2100.

[24] N. Sikdar, B. Konkena, J. Masa, W. Schuhmann, T.K. Maji, Co<sub>3</sub>O<sub>4</sub>@Co/NCNT nanostructure derived from a dicyanamide-based metal-organic framework as an efficient bi-functional electrocatalyst for oxygen reduction and evolution reactions, *Chem. - Eur. J.* 23 (2017) 18049–18056.

[25] Z. Liu, D. Ye, X. Zhu, S. Wang, Y. Zou, L. Lan, R. Chen, Y. Yang, Q. Liao, ZIF-67-derived Co nanoparticles embedded in N-doped porous carbon composite interconnected by MWCNTs as highly efficient ORR electrocatalysts for a flexible direct formate fuel cell, *Chem. Eng. J.* 432 (2022), 134192.

[26] C. Fang, Q. Yi, A. Chen, Y. Wang, X. Li, Fabrication of FeCo/multidimensional carbon-based nanocomposites as excellent cathodic catalysts of Zn-air battery, *J. Electrochem. Soc.* 169 (2022), 110538.

[27] L. Ma, R. Wang, Y.-H. Li, X.-F. Liu, Q.-Q. Zhang, X.-Y. Dong, S.-Q. Zang, Apically Co-nanoparticles-wrapped nitrogen-doped carbon nanotubes from a single-source MOF for efficient oxygen reduction, *J. Mater. Chem. A* 6 (2018) 24071–24077.

[28] Y. Li, Z. Jin, T. Zhao, Performance of ZIF-67-derived fold polyhedrons for enhanced photocatalytic hydrogen evolution, *Chem. Eng. J.* 382 (2020), 123051.

[29] K.Y. Lin, H.A. Chang, Ultra-high adsorption capacity of zeolitic imidazole framework-67 (ZIF-67) for removal of malachite green from water, *Chemosphere* 139 (2015) 624–631.

[30] E. Zhang, Y. Xie, S. Ci, J. Jia, P. Cai, L. Yi, Z. Wen, Multifunctional high-activity and robust electrocatalyst derived from metal-organic frameworks, *J. Mater. Chem. A* 4 (2016) 17288–17298.

[31] K. Aoki, R. Senga, Y. Suga, K. Totani, T. Maki, H. Itoh, K. Shinokura, K. Suenaga, T. Watanabe, Structural analysis and oxygen reduction reaction activity in bamboo-like nitrogen-doped carbon nanotubes containing localized nitrogen in nodal regions, *Carbon* 123 (2017) 99–105.

[32] B. Wen, J. Zhao, T. Li, C. Dong, J. Jin, n-Diamond from catalysed carbon nanotubes: synthesis and crystal structure, *J. Phys. -Condens. Mater.* 17 (2005) 513–519.

[33] X. Liu, W. Yang, L. Chen, Z. Liu, L. Long, S. Wang, C. Liu, S. Dong, J. Jia, Graphitic carbon nitride (g-C<sub>3</sub>N<sub>4</sub>)-derived bamboo-like carbon nanotubes/Co nanoparticles hybrids for highly efficient electrocatalytic oxygen reduction, *ACS Appl. Mater. Interfaces* 12 (2020) 4463–4472.

[34] H. Zhang, M. Zhao, H. Liu, S. Shi, Z. Wang, B. Zhang, L. Song, J. Shang, Y. Yang, C. Ma, L. Zheng, Y. Han, W. Huang, Ultrastable FeCo bifunctional electrocatalyst on Se-doped CNTs for liquid and flexible all-solid-state rechargeable Zn-air batteries, *Nano Lett.* 21 (2021) 2255–2264.

[35] B.Y. Xia, Y. Yan, N. Li, H.B. Wu, X.W.D. Lou, X. Wang, A metal-organic framework-derived bifunctional oxygen electrocatalyst, *Nat. Energy* 1 (1) (2016) 8.

[36] M. Zhu, C. Zhang, FeCo nanoalloys encapsulated in pod-like N-doped carbon nanotubes as efficient oxygen reduction reaction electrocatalysts for zinc-air batteries, *J. Alloys Compd.* 921 (2022), 166122.

[37] W. Li, B. Liu, D. Liu, P. Guo, J. Liu, R. Wang, Y. Guo, X. Tu, H. Pan, D. Sun, Alloying Co species into ordered and interconnected macroporous carbon polyhedra for efficient oxygen reduction reaction in rechargeable zinc-air batteries, *Adv. Mater.* 34 (2022), 2109605.

[38] H. Wang, L. Wei, J. Liu, J. Shen, Hollow bimetal ZIFs derived Cu/Co/N co-coordinated ORR electrocatalyst for microbial fuel cells, *Int. J. Hydrogen Energy* 45 (2020) 4481–4489.

[39] N. Sikdar, B. Konkena, J. Masa, W. Schuhmann, T.K. Maji, Co(3)O.(4) @Co/NCNT nanostructure derived from a dicyanamide-based metal-organic framework as an efficient bi-functional electrocatalyst for oxygen reduction and evolution reactions, *Chemistry* 23 (2017) 18049–18056.

[40] F. Qin, P. Zuo, N. Li, S. Qu, W. Shen, 3D flower-like carbon spheres with hierarchical pore structure: an efficient asphaltene-based metal-free catalyst for ORR, *Adv. Mater. Interfaces* 9 (2022), 2201157.

[41] Y.W. Li, W.J. Zhang, J. Li, H.Y. Ma, H.M. Du, D.C. Li, S.N. Wang, J.S. Zhao, J. M. Dou, L. Xu, Fe-MOF-derived efficient ORR/OER bifunctional electrocatalyst for rechargeable zinc-air batteries, *ACS Appl. Mater. Interfaces* 12 (2020) 44710–44719.

[42] Q. Lai, J. Zheng, Z. Tang, D. Bi, J. Zhao, Y. Liang, Optimal configuration of N-doped carbon defects in 2D turbostratic carbon nanomesh for advanced oxygen reduction electrocatalysis, *Angew. Chem. Int. Ed. Engl.* 59 (2020) 11999–12006.

[43] B. Wen, J.J. Zhao, T.J. Li, Synthesis and crystal structure of n-diamond, *Int. Mater. Rev.* 52 (2013) 131–151.

[44] P. Song, Y. Wang, J. Pan, W. Xu, L. Zhuang, Structure-activity relationship in high-performance iron-based electrocatalysts for oxygen reduction reaction, *J. Power Sources* 300 (2015) 279–284.

[45] K. He, J. Zai, X. Liu, Y. Zhu, A. Iqbal, T. Tadesse Tsega, Y. Zhang, N. Ali, X. Qian, One-step construction of multi-doped nanoporous carbon-based nanoarchitecture as an advanced bifunctional oxygen electrode for Zn-Air batteries, *Appl. Catal. B: Environ.* 265 (2020), 118594.

[46] J. Xiao, J.L. Li, P. Liu, G.W. Yang, A new phase transformation path from nanodiamond to new-diamond via an intermediate carbon onion, *Nanoscale* 6 (2014) 15098–15106.

[47] B. Wang, C.-Y. Shu, C.-R. Wang, Metal-free preparation of multi-walled carbon nanotubes based on new-diamond-induced growth mechanism, *J. Mater. Chem.* (2010) 7104–7106.

[48] T. Xu, S. Yang, J. Lu, Q. Xue, J. Li, W. Guo, Y. Sun, Characterization of nanocrystalline diamond films implanted with nitrogen ions, *Diam. Relat. Mater.* 10 (2001) 1441–1447.

[49] Z. Sun, Y. Sun, S. Wilson, An amorphous hydrocarbon diamond-like polymer as a precursor for diamond growth, *Thin Solid Films* 377 (2000) 203–207.

[50] J.S. Li, S.L. Li, Y.J. Tang, M. Han, Z.H. Dai, J.C. Bao, Y.Q. Lan, Nitrogen-doped Fe/Fe<sub>3</sub>C/graphitic layer/carbon nanotube hybrids derived from MOFs: efficient bifunctional electrocatalysts for ORR and OER, *Chem. Commun. (Camb.)* 51 (2015) 2710–2713.

[51] A. Chen, Q. Yi, K. Sheng, Y. Wang, J. Chen, Q. Zhang, K. Xiang, G. Tan, Mesoporous N-P codoped carbon nanosheets as superior cathodic catalysts of neutral metal-air batteries, *Langmuir* 37 (2021) 12616–12628.

[52] Z. Liu, D. Ye, X. Zhu, S. Wang, Y. Zou, L. Lan, R. Chen, Y. Yang, Q. Liao, ZIF-67-derived Co nanoparticles embedded in N-doped porous carbon composite

interconnected by MWCNTs as highly efficient ORR electrocatalysts for a flexible direct formate fuel cell, *Chem. Eng. J.* 432 (2022), 134192.

[53] C. Feng, Y. Guo, S. Qiao, Y. Xie, L. Zhang, L. Zhang, W. Wang, J. Wang, 2-Methylimidazole as a nitrogen source assisted synthesis of a nano-rod-shaped Fe/FeN@N-C catalyst with plentiful FeN active sites and enhanced ORR activity, *Appl. Surf. Sci.* 533 (2020), 147481.

[54] Y. Wang, R. Yi, A. Chen, C. Fang, Y. Wang, Q. Yi, M. Liu, S. Liu, S. Zhan, B. Zhong, Hollow carbon sphere and polyhedral carbon composites supported iron nanoparticles as excellent bifunctional electrocatalysts of Zn-air battery, *Energy Technol.* 10 (2022), 2200057.

[55] S.S.A. Shah, T. Najam, C. Cheng, L. Peng, R. Xiang, L. Zhang, J. Deng, W. Ding, Z. Wei, Exploring Fe-Nx for peroxide reduction: template-free synthesis of Fe-N<sub>x</sub> traumatised mesoporous carbon nanotubes as an ORR catalyst in acidic and alkaline solutions, *Chem. Eur. J.* 24 (2018) 10630–10635.

[56] C. Karaman, Orange peel derived-nitrogen and sulfur Co-doped carbon dots: a nano-booster for enhancing ORR electrocatalytic performance of 3D graphene networks, *Electroanalysis* 33 (2021) 1356–1369.

[57] F. Kong, X. Cui, Y. Huang, H. Yao, Y. Chen, H. Tian, G. Meng, C. Chen, Z. Chang, J. Shi, N-doped carbon electrocatalyst: marked ORR activity in acidic media without the contribution from metal sites? *Angew. Chem. Int. Ed.* 61 (2022), e202116290.

[58] M.X. Chen, M. Zhu, M. Zuo, S.Q. Chu, J. Zhang, Y. Wu, H.W. Liang, X. Feng, Identification of catalytic sites for oxygen reduction in metal/nitrogen-doped carbons with encapsulated metal nanoparticles, *Angew. Chem. Int. Ed. Engl.* 59 (2020) 1627–1633.

[59] X.R. Wang, J.Y. Liu, Z.W. Liu, W.C. Wang, J. Luo, X.P. Han, X.W. Du, S.Z. Qiao, J. Yang, Identifying the key role of pyridinic-N-Co bonding in synergistic electrocatalysis for reversible ORR/OER, *Adv. Mater.* (2018) 30, e1800005.

[60] H.-T. Fang, C.-G. Liu, C. Liu, F. Li, M. Liu, H.-M. Cheng, Purification of single-wall carbon nanotubes by electrochemical oxidation, *Chem. Mater.* 16 (2004) 5744–5750.

[61] X. Tang, R. Cao, L. Li, B. Huang, W. Zhai, K. Yuan, Y. Chen, Engineering efficient bifunctional electrocatalysts for rechargeable zinc-air batteries by confining Fe-Co-Ni nanoalloys in nitrogen-doped carbon nanotube@nanosheet frameworks, *J. Mater. Chem. A* 8 (2020) 25919–25930.

[62] X. Hao, Z. Jiang, B. Zhang, X. Tian, C. Song, L. Wang, T. Maiyalagan, X. Hao, Z. J. Jiang, N-doped carbon nanotubes derived from graphene oxide with embedment of FeCo nanoparticles as bifunctional air electrode for rechargeable liquid and flexible all-solid-state zinc-air batteries, *Adv. Sci.* 8 (2021), 2004572.

[63] R. Yuan, W. Bi, T. Zhou, N. Zhang, C.A. Zhong, W. Chu, W. Yan, Q. Xu, C. Wu, Y. Xie, Two-dimensional hierarchical Fe-N-C electrocatalyst for Zn-air batteries with ultrahigh specific capacity, *ACS Mater. Lett.* 2 (2019) 35–41.

[64] I.S. Amiinu, X. Liu, Z. Pu, W. Li, Q. Li, J. Zhang, H. Tang, H. Zhang, S. Mu, From 3D ZIF nanocrystals to Co-N<sub>x</sub>/C nanorod array electrocatalysts for ORR, OER, and Zn-air batteries, *Adv. Funct. Mater.* 28 (2018), 1704638.